Journal of
Synchrotron
Radiation

ISSN 1600-5775

Received 6 January 2014
Accepted 2 September 2014

Cooling dynamics of self-assembled monolayer coating for integrated gold nanocrystals on a glass substrate

Kouhei Ichiyanagi,[a]* Hiroshi Sekiguchi,[b] Tokushi Sato,[c] Shunsuke Nozawa,[c] Ayana Tomita,[c] Manabu Hoshino,[d] Shin-ichi Adachi[c] and Yuji C. Sasaki[a]

[a]Photon Factory, Institute of Materials Structure Science, High Energy Accelerator Research Organization, 1-1 Oho, Tsukuba, Ibaraki 305-0801, Japan, [b]Japan Synchrotron Radiation Research Institute (JASRI), SPring-8, 1-1 Sayo, Hyogo 679-5198, Japan, [c]Deutsches Elektronen-Synchrotron (DESY), 85 Notkestrasse, Hamburg 22607, Germany, and [d]Department of Chemistry and Materials Science, Tokyo Institute of Technology, Meguro-ku, Tokyo 152-8551, Japan.
*E-mail: kouhei.ichiyanagi@kek.jp

Picosecond time-resolved X-ray diffraction has been used to study the nanoscale thermal transportation dynamics of bare gold nanocrystals and thiol-based self-assembled monolayer (SAM)-coated integrated gold nanocrystals on a SiO_2 glass substrate. A temporal lattice expansion of 0.30–0.33% was observed in the bare and SAM-coated nanocrystals on the glass substrate; the thermal energy inside the gold nanocrystals was transported to the contacted substrate through the gold–SiO_2 interface. The interfacial thermal conductivity between the single-layered gold nanocrystal film and the SiO_2 substrate is estimated to be 45 MW m^{-2} K^{-1} from the decay of the Au 111 peak shift, which was linearly dependent on the transient temperature. For the SAM-coated gold nanocrystals, the thermal dissipation was faster than that of the bare gold nanocrystal film. The thermal flow from the nanocrystals to the SAM-coated molecules promotes heat dissipation from the laser-heated SAM-coated gold nanocrystals. The thermal transportation of the laser-heated SAM-coated gold nanocrystal film was analyzed using the bidirectional thermal dissipation model.

Keywords: time-resolved X-ray diffraction; thermal conductance; nanocrystal; thermal flow.

1. Introduction

Nanoscale heat transfer has attracted growing interest in terms of the fundamental understanding of thermal transport phenomena at the nanoscale interface (Cahill *et al.*, 2001, 2003; Pernot *et al.*, 2010; Losego *et al.*, 2012). The control of thermal flow from hot-spotted nanodevices on the substrate or on some attached interfaces in use is an especially important issue for nanodevice design. Nanomaterials deteriorate, and chemical reactions, phase transitions and material growth result from the extra thermal energy produced. The interfacial thermal conductivity on the nanomaterial interface is very dependent on size and interface structure. Nanoscale heat dissipation is influenced by an additional size effect that involves heterogeneous interface conditions (Siemens *et al.*, 2010). A design consideration for the integrated nanoscale circuit is that the excess thermal energy should be dissipated as rapidly as possible to protect these nanodevices from Joule heating during use.

Although thermal transport occurs from nanomaterial to substrate, a thermal transport path that uses a self-assembled molecular (SAM) coating on the material surface is available within nanoseconds (Ge *et al.*, 2006; Wang *et al.*, 2007; Harikrishna *et al.*, 2013). The interfacial thermal conductivity between the heat-sink substrate and the molecular coating attached to the nanomaterial surface must be taken into account for thermal flow management of nanomaterial devices.

Recently, short-pulse X-rays have been shown to be sensitive enough for observation of the lattice cooling dynamics of the interfacial thermal conductivity, and vibration within gold nanoparticles and thin films, and can be used to determine transient temperatures at the picosecond time scale (Plech *et al.*, 2003, 2004; Sheu *et al.*, 2008; Ichiyanagi *et al.*, 2011; Highland *et al.*, 2007). The lattice space changes ΔQ (Å^{-1}) are proportional to the temperature change *via* the expansion coefficient. The thermal expansion of the lattice constant through the Bragg angle shift, $\Delta Q(t)$, after heating is related directly to the transient average temperature in the nanomaterials, $\langle \Delta T(t) \rangle$, as follows:

$$\frac{\Delta Q(t)}{Q} = \alpha \langle \Delta T(t) \rangle, \qquad (1)$$

where α is the linear thermal expansion coefficient of the sample. Using time-resolved X-ray diffraction (TR-XRD), the precise temporal temperature of the thermalized nanomaterial during cooling can be obtained in a characteristic delay time (Plech *et al.*, 2003, 2004; Sheu *et al.*, 2008, 2011). Thus far, the thermal transport of individual metal nanoparticles in colloidal solution or embedded glass and thin layers has been measured using the thermal diffusivity of the environmental matrix and the thermal interfacial conductivity has been measured using TR-XRD and thermoreflectance (Plech *et al.*, 2003, 2004; Sheu *et al.*, 2008; Hartland, 2002; Hu & Hartland, 2002; Banfi *et al.*, 2012; Juvé *et al.*, 2009).

In this work we report on our direct observation of the heat transport phenomena of integrated bare gold nanocrystal films and SAM-coated gold nanocrystal films on a SiO_2 glass substrate using picosecond TR-XRD.

2. Preparation of single-layered gold nanocrystals film

A single layer of fine crystallized gold nanocrystals was produced on a bulk SiO_2 glass surface (40 µm thickness) using vapor deposition and annealing (Okumura *et al.*, 2005). We estimated the conformation and distribution of gold nanocrystals on the substrate using atomic force microscopy (AFM), as shown in Figs. 1(*a*) and 1(*b*). The single-layered gold nanocrystals on the substrate are in contact with the neighboring gold nanocrystals. The average size distribution of the gold nanocrystals was estimated to be 13 ± 3 nm from the AFM image. The average height of the gold nanocrystals was 13 nm. The SAM-coated gold nanocrystal films were prepared by immersing the bare films in a 10 m*M* solution of 10-dodecacarboyl disulfide (DCDS) in ethanol for 1 h. In the SAM-coated gold nanocrystals the sample spacer used to hold the buffer solution was a 50 µm-thick polyimide film. The fused quartz glass cover, the spacer and the sample film were held by a metal frame with a 7 mm^2 window.

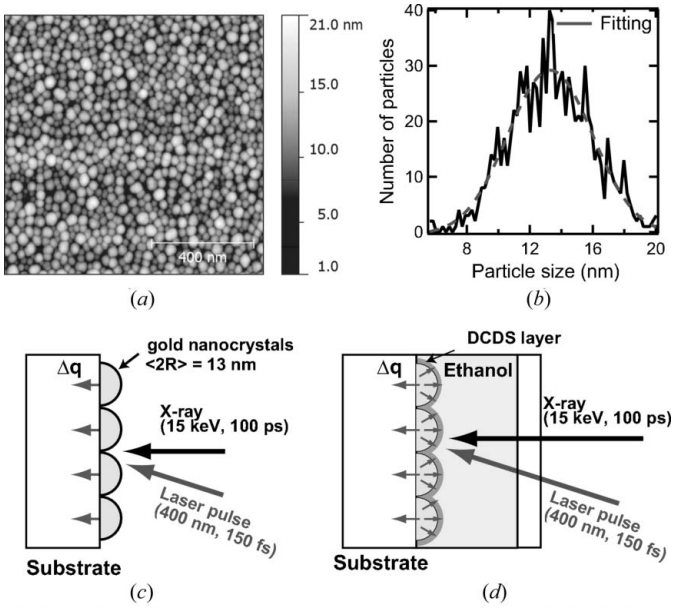

Figure 1
(*a*) Tapping-mode AFM image of bare gold nanocrystals on fused quartz substrate. (*b*) The gold nanocrystal size distribution was estimated from (*a*); the mean size of the gold nanocrystals was 13 ± 3 nm. (*c*) Single-layered bare gold nanocrystals on the fused quartz substrate. (*d*) Single-layered self-assembled molecules coated on gold nanocrystal surface and immersed in ethanol solution. Arrows from gold nanocrystals indicate the flow direction of thermal energy (Δq) from femtosecond laser-heated gold nanocrystals.

3. Experimental set-up

We performed TR-XRD measurements on the NW14A beamline at the Photon Factory-Advanced Ring, KEK, in Tsukuba, Japan. A detailed description of this beamline can be found elsewhere (Nozawa *et al.*, 2007; Ichiyanagi *et al.*, 2011). A pump laser from a Ti:sapphire regenerative amplifier system with a 150 fs pulse was used to excite the single-layered gold nanocrystal film at 946 Hz. The excitation wavelength for gold nanocrystals was 400 nm, which was generated through the frequency doubling in a 1 mm-thick barium borate crystal from 800 nm. The laser fluence for exciting the gold nanocrystals was 3 mJ cm^{-2}. Laser-induced melting and the dissociation of molecules at the surface does not occur at this fluence. The X-ray pulse for probing lattice changes inside the gold nanocrystals was characterized with monochromatic X-rays of 15 keV and a pulse width of 100 ps, which was synchronized with the laser at 946 Hz. The focusing spot size of the X-ray and laser at the sample position was 0.45 mm × 0.25 mm with a 1 mm diameter. The sample was fixed perpendicular to the X-ray and laser. The laser path was approximately 10° in front of the X-ray path. We observed the two-dimensional powder X-ray diffraction pattern of gold nanocrystals by transmission geometry, as shown in Figs. 1(*c*) and 1(*d*). The X-ray diffraction patterns were recorded using a charge-coupled device (MarCCD165, MarUSA, Evanton, IL, USA) of diameter 165 mm.

4. Result and discussion

The X-ray diffraction profile of bare gold nanocrystals and SAM-coated gold nanocrystals on the SiO_2 substrate was obtained using the area detector at each delay time. The diffraction pattern displayed Debye–Scherrer symmetry, which indicates that the gold nanocrystals are oriented randomly on the substrate, as shown in Fig. 2(*a*). The inner broadened scattering is the first sharp diffraction peak of silicate glass attributed to an intermediate-ordered structure. We changed the Debye–Scherrer ring to a one-dimensional diffraction profile. Fig. 2(*b*) shows that the diffraction peak of Au 111 inside the gold nanocrystals shifted to the lower angle side after laser-induced thermalization. The gold nanocrystals were of the face-centered-cubic structure, which is the same as bulk gold. Fig. 2(*b*) shows profiles of gold 111 diffraction peaks with broadening by the size effect at −120 and 180 ps. All of the gold nanocrystals expanded suddenly within a few picoseconds after the electron–phonon coupling because of the excitation of local surface plasmon resonance by femtosecond laser pulse at 400 nm (Hodak *et al.*, 1999; Inouye *et al.*, 1998;

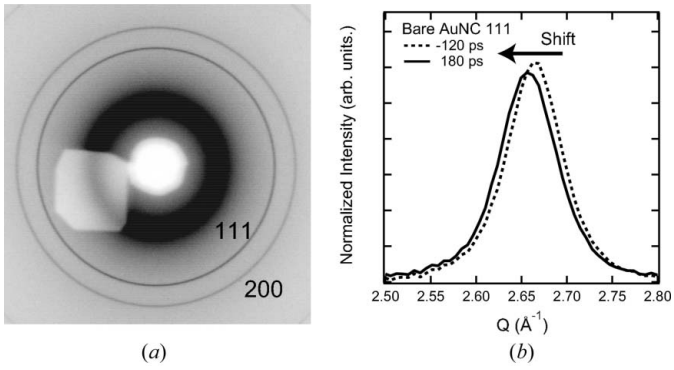

Figure 2
(*a*) Two-dimensional X-ray diffraction image of single-layered bare gold nanocrystals on the substrate. The inner diffused scattering is from the amorphous silica glass structure. (*b*) Profiles of the Au 111 diffraction peak for single-layered bare gold nanocrystals before laser irradiation at −120 ps (dotted line) and after femtosecond laser irradiation at 180 ps (solid line).

Hopkins *et al.*, 2009). Then, the thermal energy in the laser-heated gold nanocrystals passed through the SiO_2 glass substrate through the Au–SiO_2 glass interface. We estimated the peak position at each time delay by fitting a Gaussian function.

From changes in the Au 111 lattice constant, we estimated the time-dependent average temperature inside the gold nanocrystals. Fig. 3 displays the cooling dynamics after laser heating changes of bare and SAM-coated gold nanocrystals. The estimated transient average temperatures (ΔT) were derived using the thermal expansion coefficient of bulk gold, $\alpha = 14.4 \pm 10^{-6}\,K^{-1}$, $\Delta d/d = \alpha \Delta T$ using equation (1). The maximum temperature of bare and SAM-coated gold nanocrystals at 180 ps is about 250 K. With this extra heat dissipation route, the cooling rate of the SAM-coated gold nanocrystal films was faster than that of the bare gold nanocrystal films. A laser-induced acoustic pulse, such as an elastic shock wave, in the nanosecond time scale is too short to be observed using this time resolution. The coherent vibration inside the nanoparticles depends on size and shape. The vibration period of the 13 nm gold nanoparticles is below 100 ps. The initial thermalization rise-down time and coherent vibration was convoluted with the 100 ps X-ray pulse (Nozawa *et al.*, 2010). The thermalization process and coherent vibration occur within a few picoseconds, which is shorter than the X-ray pulse (Hodak *et al.*, 1999; Hartland, 2002). In addition, we observed that the peak width relaxation occurs on a smaller time scale than the peak shift relaxation, as shown in the inset of Fig. 3. This peak broadening phenomenon indicates that the monolayer gold nanocrystals expanded non-uniformly perpendicular and parallel to the monolayer surface and that the coherent lattice vibration has an insufficient vibration period (Plech *et al.*, 2003). The cooling dynamics of bare and SAM-coated gold nanocrystals exhibit a non-exponential decay of the measured peak shift of Au 111 as observed using TR-XRD.

The thermal energy in the bare gold nanocrystals is transported to the substrate through the gold–SiO_2 glass substrate

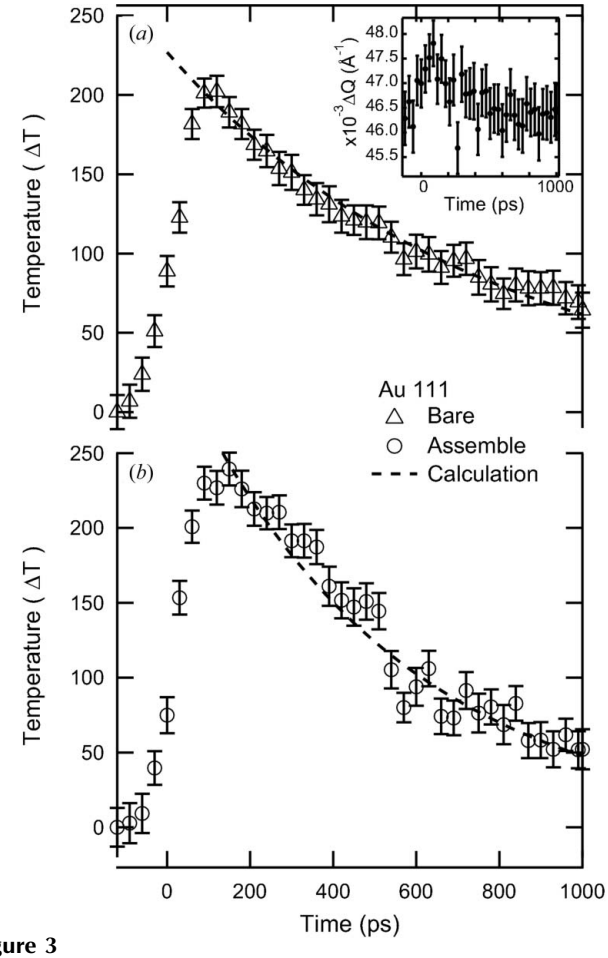

Figure 3
Time-dependent temperature changes of the Au 111 lattice in the single-layered bare gold [(*a*) open triangles] and SAM-coated gold nanocrystals [(*b*) open circles] after femtosecond laser excitation. Dotted lines show the characteristic time decay of cooling dynamics in the thermalized gold nanocrystals calculated using experimental data with equations (2) and (3). (Insert) Time-dependence of peak width, ΔQ, of single-layered bare gold nanocrystals.

(Fig. 1*a*). In contrast, the thermal energy of the SAM-coated gold nanocrystals is transported not only to the gold–SiO_2 glass substrate but also to the gold–DCDS through covalent bonding (Fig. 1*b*). Therefore, the cooling rate of SAM-coated gold nanocrystals is faster than that of bare gold nanocrystal films. For the SAM-coated gold nanocrystal films, the laser-induced heat energy in the gold nanocrystals can be transported into the substrate and the attached SAM through each interface. The attached DCDS molecules on the surface accelerate the cooling rate.

After interpreting the nanosecond heat flow from the monolayer gold nanocrystals supported on the glass substrate, we considered the interfacial thermal conductivity at the interfaces and thermal diffusive process in the support glass substrate. First, we analyzed the cooling dynamics of monolayer gold nanocrystals supported on the SiO_2 substrate using two equations of the interfacial thermal conductivity between the gold–SiO_2 and the thermal diffusion process into the support substrate from the molecular-attached substrate surface.

The cooling dynamics through the interfaces of the gold nanocrystal–SiO_2 glass substrate and the thermal diffusion into the substrate was assumed to exhibit one-dimensional heat flow geometry. We implemented the formula for the heat flow at the interfaces of the gold nanocrystal–SiO_2 and the gold nanocrystal–SAM-coated molecules as follows:

$$hC_n \frac{dT}{dt} = -G_1\left[T_n(t) - T_s(t, z = 0)\right] - G_2\left[T_n(t) - T\right], \quad (2)$$

where G_1, G_2, h, C_n, $T_n(t)$ and $T_s(t, z)$ are the interfacial thermal conductivity between the gold nanocrystals and the substrate, the interfacial thermal conductivity between the gold nanocrystals and the SAM-coated molecules, the film thickness of the gold nanocrystals, the volumetric heat capacity of gold, the instantaneous temperature and the substrate temperature, respectively. In addition, heat diffusion in the SiO_2 glass substrate is solved numerically by the normal heat diffusion equation:

$$C_s \frac{dT(t, z)}{dt} = \kappa_s \frac{d^2T(t)}{dz^2}, \quad (3)$$

where C_s and κ_s are the volumetric heat capacity and the thermal conductivity of SiO_2 glass. For the cooling dynamics of bare gold nanocrystal films, the second term in equation (2) can be ignored. First, we estimated G_1 using from the cooling dynamics of bare gold nanocrystal films using (2) (excluding the second term) and (3). Then we analyzed the bidirectional cooling dynamics of SAM-coated gold nanocrystal films using (2) and (3) with an estimated G_1 value.

The best fit for interfacial thermal conductivity at the gold nanocrystal–SiO_2 interface is 45 MW m^{-2} K^{-1} from the bare gold nanocrystal film data, as shown in Fig. 3(*a*). Smith *et al.* reported that the interfacial thermal conductivity of gold thin film (30 nm thickness) on SiO_2 glass substrate was 56 MW m^{-2} K^{-1} as probed by the femtosecond laser pump–probe method (Smith *et al.*, 2000). Our analytical value was slightly lower than the interfacial thermal conductivity of the uniform gold thin film evaporating on the SiO_2 glass substrate. The heat flux phonon from the gold nanocrystal films to the SiO_2 glass substrate diffused at its heterogeneous interfaces. In addition, this value was half that of the interfacial thermal conductivity of the glass-embedded gold nanoparticles (Juvé *et al.*, 2009). The effective contact area between the gold nanocrystals and the SiO_2 glass substrate is much lower than for the glass-embedded gold nanoparticles, which are in contact with the surrounding SiO_2 glass media. The thermal transport of monolayer gold nanoparticles is much closer to that of the thin gold film.

For the SAM-coated gold nanocrystal films (Fig. 3*b*), the total thermal energy of the gold nanocrystals changes at the rate that heat is also transferred from the nanocrystal films to the SAM molecule layer and the ethanol solution. Heat flow from the gold surface into the attached molecules was assumed to be almost constant throughout the cooling dynamics. For a numerical analysis of the cooling rate of SAM-coated gold nanocrystal films, the heat flow across the gold–SAM interface decays exponentially. We analyzed the cooling dynamics of SAM-coated gold nanocrystal films using equations (2) and (3). The value of the interfacial thermal conductivity at the interface between the gold nanocrystal film surface and the thiols on the surface is 22 MW m^{-2} K^{-1}, which was estimated from $G = hC/\tau$. The estimated parameter is the decay time of the cooling dynamics from the nanocrystal surface to the SAM and ethanol solution, τ. The characteristic decay time was estimated to be 0.7×10^9 s^{-1}. The gold nanocrystal–thiol interface helps dissipate extra heat in nanoseconds. The heat flow dynamics of integrated SAM-coated gold nanocrystal films was described very well by the bidirectional heat diffusion model on the nanoscale film. Coating of self-assembled molecules on integrated metal island nanomaterials on the substrate can act as nanosized heat sinks for functionalized nanodevices using nanocircuits.

5. Summary

In summary, we have measured the bidirectional thermal transport dynamics of bare gold nanocrystal films with SAM-coated gold nanocrystal films using picosecond TR-XRD. By establishing the extra heat flow route using molecular modification on the nanomaterial surface, we have demonstrated the effect of efficient thermal transport of heated nanomaterials on the substrate in the nanosecond time scale. The thermal flow dynamics of bare and SAM-coated gold nanocrystal films has been well described as thermal diffusion inside the gold nanocrystals on the subnanosecond timescale.

This work was performed with the approval of the Photon Factory Advisory Committee (proposals No. 2011G631 and 2013G624) and was supported by the Futaba Electric Memorial Foundation.

References

Banfi, F., Juvé, V., Nardi, D., Conte, S. D., Giannetti, C., Ferrini, G., Fatti, N. D. & Vallee, F. (2012). *Appl. Phys. Lett.* **100**, 011902.
Cahill, D. G., Ford, W. K., Goodson, K. E., Mahan, G. D., Majumdar, A., Maris, H. J., Merlinm, R. & Phillpot, S. R. (2003). *J. Appl. Phys.* **93**, 793–818.
Cahill, D. G., Goodson, K. E. & Majumdar, A. (2001). *J. Heat Transfer*, **124**, 223–241.
Ge, Z., Cahill, D. G. & Braun, P. V. (2006). *Phys. Rev. Lett.* **96**, 186101.
Harikrishna, H., Ducker, W. A. & Huxtable, S. T. (2013). *Appl. Phys. Lett.* **102**, 251606.
Hartland, G. V. (2002). *J. Chem. Phys.* **116**, 8048–8055.
Highland, M., Gundrum, B. C., Koh, Y. K., Averback, R. S. & Cahill, D. G. (2007). *Phys. Rev. B*, **76**, 075337.
Hodak, J. H., Henglien, A. & Hartland, G. V. (1999). *J. Chem. Phys.* **111**, 8613–8621.
Hopkins, P. E., Kassebaum, J. L. & Norris, P. M. (2009). *J. Appl. Phys.* **105**, 023710.
Hu, M. & Hartland, G. V. (2002). *J. Phys. Chem.* **106**, 7029–7033.
Ichiyanagi, K., Sekiguchi, H., Nozawa, S., Sato, T., Adachi, S. & Sasaki, Y. C. (2011). *Phys. Rev. B*, **84**, 024110.
Inouye, H., Tanaka, K., Takahashi, I. & Hirao, K. (1998). *Phys. Rev. B*, **57**, 11134–11340.
Juvé, V., Scardamaglia, M., Maioli, P., Crut, A., Merabia, S., Joly, L., Fatti, N. D. & Vallee, F. (2009). *Phys. Rev. B*, **80**, 195406.
Losego, M. D., Grady, M. E., Sottos, N. R., Cahill, D. G. & Braun, P. V. (2012). *Nat. Mater.* **11**, 502–506.

Nozawa, S., Adachi, S., Takahashi, J., Tazaki, R., Guérin, L., Daimon, M., Tomita, A., Sato, T., Chollet, M., Collet, E., Cailleau, H., Yamamoto, S., Tsuchiya, K., Shioya, T., Sasaki, H., Mori, T., Ichiyanagi, K., Sawa, H., Kawata, H. & Koshihara, S. (2007). *J. Synchrotron Rad.* **14**, 313–319.
Nozawa, S., Sato, T., Chollet, M., Ichiyanagi, K., Tomita, A., Fujii, H., Adachi, S. & Koshihara, S. Y. (2010). *J. Am. Chem. Soc.* **132**, 61–63.
Okumura, Y., Miyazaki, T., Taniguchi, Y. & Sasaki, Y. C. (2005). *Thin Solid Films*, **471**, 91–95.
Pernot, G., Stoffel, M., Savic, I., Pezzoli, F., Chen, P., Savelli, S., Jacquot, A., Schumann, J., Denker, U., Mönch, I., Denke, Ch., Schmidt, O. G., Rampnoux, J. M., Wang, S., Plissonnier, M., Rasteli, A., Dihaire, S. & Mingo, N. (2010). *Nat. Mater.* **9**, 491–495.
Plech, A., Kotaidis, V., Gresillon, S., Dahmen, C. & von Plesson, G. (2004). *Phys. Rev. B*, **70**, 195423.
Plech, A., Kurbiz, S., Berg, K.-J., Graener, H., Gresillon, S., Kaempfe, M., Feldmann, J., Eulf, M. & von Lesson, G. (2003). *Europhys. Lett.* **61**, 762–768.
Sheu, Y. M., Lee, S. H., Wahlstrand, J. K., Walko, D. A., Landhal, E. C., Arms, D. A., Reason, M., Coldman, R. S. & Reis, D. A. (2008). *Phys. Rev. B*, **78**, 045317.
Sheu, Y. M., Trigo, M., Chien, Y. J., Uher, C., Arms, D. A., Peterson, E. R., Walko, D. A., Landahl, E. C., Chen, J., Ghimire, S. & Reis, D. A. (2011). *Solid State Commun.* **151**, 826–829.
Siemens, M., Li, Q., Yang, R., Nelson, K., Anderson, E., Murnane, M. & Kapteyn, H. (2010). *Nat. Mater.* **9**, 26–30.
Smith, A. N., Hostetler, J. H. & Norris, P. M. (2000). *Microscale Thermophys. Eng.* **4**, 51–60.
Wang, Z., Carter, J. A., Lagutchev, A., Koh, Y. K., Seong, N. H., Cahill, D. G. & Dlott, D. D. (2007). *Science*, **317**, 787–790.